Scientia Iranica, Vol. 15, No. 1, pp 108–119

SCIENTIA
IRANICA

Enhancement of Natural Convection in Circular and Triangular Ducts Using Corona Discharge in Air and Nitrogen

M. Molki* and T. Harirchian[1]

A computational effort is undertaken to investigate the effect of corona discharge in air and nitrogen gas on the enhancement of heat transfer. A corona is a visible luminous emission that occurs in the vicinity of sharp edges where the electric field is intense. This phenomenon is associated with gas ionization and acceleration of ions in strong electric fields, dragging the gas particles and generating a secondary flow, known as corona wind. Corona wind may be employed as an active enhancement technique for heat transfer. Here, corona wind is used to enhance natural convection inside circular tubes and triangular ducts. The paper describes, not only the enhancement of heat transfer, but also, the shortcoming and challenges encountered in the computational modeling of corona discharge. It is shown that the solution of the electric charge density suffers from some degree of irregularity and asymmetry, while an azimuthally symmetric solution is expected. If this deficiency is not rectified, the resulting electric body force and the predicted flow field are not accurate. Two remedies are recommended to improve the solution, namely, artificial viscosity and structured grids. Moreover, the present computations indicate that, for the Rayleigh number of 3737 and the applied voltage of 8.25-9.5 kV, the corona discharge enhances heat transfer by 17.9-106.9.

INTRODUCTION

Circular and triangular ducts are widely used as flow passages in heat transfer devices. The fluid is often driven by a pump through an array of ducts and the thermal energy is transported via forced convection. In the case of power outage, forced convection stops and natural convection becomes the dominant mode of heat transfer. Having a low heat transfer coefficient, natural convection is not an effective mode of heat transfer, and it needs to be enhanced using an enhancement technique. From among many available techniques, generation of a secondary flow by corona discharge is an active technique for the enhancement of heat transfer in both internal and external flows. This paper is intended to present the level of enhancement achieved by this technique. The emphasis of the work, however, is on the difficulties and challenges encountered in modeling corona discharge in circular and triangular ducts, and the remedies to improve the solution of the associated electric and flow fields.

Corona is a visible luminous emission caused by the creation of photons. This occurs in the vicinity of sharp edges where the intensity of the electric field is high. An important aspect of corona discharge is the generation of corona wind, which is a gas flow induced by corona discharge. This phenomenon is caused by the ionization of gas molecules and formation of electrons that accelerate in strong electric fields and collide with neutral molecules, resulting in more ionization. The ions are heavier than electrons; they accelerate and drag the neighboring gas molecules. This generates a secondary flow, known as corona wind. In this research, corona wind of air and nitrogen gas is used to enhance heat transfer in circular and triangular ducts.

Extensive research has been performed on corona discharge by engineers and physicists and there is a

*. *Corresponding Author, Department of Mechanical and Industrial Engineering, Southern Illinois University Edwardsville, Edwardsville, Illinois 62026-1805, USA.*

1. *Department of Mechanical and Industrial Engineering, Southern Illinois University Edwardsville, Edwardsville, Illinois 62026-1805, USA.*

wealth of published literature on the subject. However, the literature on the application of corona wind for the enhancement of heat transfer is more limited [1-15]. The physics and applications of corona wind for the enhancement of heat transfer have been reviewed by Molki and Bhamidipati [16].

The enhancement of convective heat transfer in the developing and fully developed regions of square ducts using corona discharge in air for laminar, as well as transitional and turbulent flows, has been studied by Molki et al. [12] and Molki and Damronglerd [17]. The available literature on corona discharge in triangular ducts, however, is seemingly scarce. Some aspects of the corona modeling, the solution of electrodynamics equations and the enhancement of natural convection in circular and triangular ducts have been investigated [18-20]. It has been shown that this technique may be employed to enhance natural convection heat transfer as much as 40% in air and 106.9% in nitrogen.

The purpose of this paper is to present the difficulties and challenges encountered in modeling corona discharge in internal flows, such as circular tubes and triangular ducts, and to recommend remedies to improve the solution. In both geometries, the electrode is a stretched wire placed at the center of the tube or duct. High voltage is applied to the electrode to generate corona discharge and secondary flow and to enhance heat transfer.

The present work is primarily computational. However, due to the complexity of the corona discharge phenomenon, an experimental setup is used to generate and measure corona current, which is, subsequently, used in the computations.

The difficulties arising from the solution of corona models are related to the numerical solution of the electric charge density equation. As shown later in this paper, the solution of a charge density may not be smooth, leading to an irregular body force, which, in turn, results in an erroneous or asymmetrical flow field. The recommended remedies are the use of artificial viscosity and a structured grid. It is shown that adding a judicious amount of artificial viscosity to the charge density equation improves the solution. The use of a structured grid, as opposed to an unstructured gird, is also beneficial and improves the solution.

GOVERNING EQUATIONS

The circular and triangular cross sections of the duct are shown in Figure 1. The electrode is located at the geometric center of the cross section. The electrode diameter is $d = 0.254$ mm for the circular tube filled with air, 0.254 mm for the triangular duct filled with air, and 0.5 mm for the triangular duct filled with nitrogen gas. The electrode is charged with positive DC voltage and the walls are electrically grounded. The

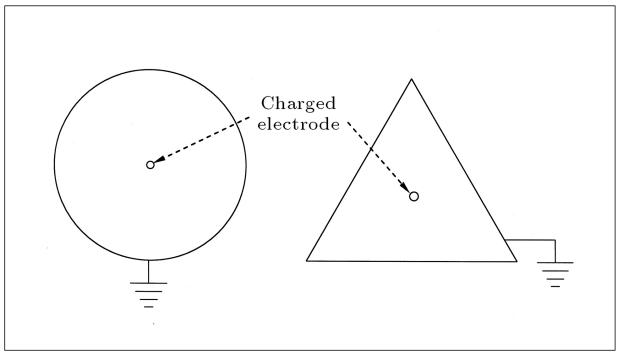

Figure 1. Cross sections of the circular tube and the triangular duct.

diameter of the circle is $D = 25.4$ mm. The hydraulic diameter of the triangle is $D_h = 25.4$ mm and 17.32 mm for the corona discharge in air and nitrogen gas, respectively. The triangle is equilateral with height $H = 38.1$ mm and 25.98 mm and base $L = 44$ mm and 30 mm for corona discharge in air and nitrogen gas, respectively. The space between the electrode and the walls is filled with air or nitrogen gas; air for the circular tube and air or nitrogen for the triangular duct.

The electrodynamics equations are solved for both circular and triangular cross sections, but the flow equations are solved only for the triangle. The right and left walls of the triangular cross section are maintained at uniform temperatures $T_h = 302$ K and $T_c = 300$ K, respectively. The lower wall is adiabatic. The origin of the system of coordinates is located on the electrode at the geometric center of the cross section, with 'x' horizontal and 'y' vertical.

The electric field is formulated by Gauss's law:

$$\partial_i D_i = \rho_c, \tag{1}$$

and by the conservation of electric charge:

$$\partial_o \rho_c + \partial_i J_i = 0, \tag{2}$$

where the displacement vector is $D_i = \varepsilon E_i$, electric field intensity is $E_i = -\partial_i V$ and current density is $J_i = \rho_c b E_i + \sigma E_i + \rho_c u_i$. Ignoring the charge convection, $\rho_c u_i$, and electric conduction, σE_i, D_i and J_i are substituted into Equations 1 and 2 and a constant permittivity is assumed to obtain the potential and charge density equations as follows:

$$\partial_i \partial_i V = -\rho_c/\varepsilon, \tag{3}$$

and:

$$\partial_o \rho_c + \partial_i(-\rho_c b \partial_i V) = 0. \tag{4}$$

The electrodynamics equations to be solved are Equations 3 and 4. Equation 3 is elliptic and needs two boundary conditions, while Equation 4 is hyperbolic,

requiring only one boundary condition. The boundary conditions for these equations are the voltage, $V = V_e$ (kV), on the electrode, $V = 0$ (kV), on the grounded walls, and the charge density, $\rho_c = \rho_{c,e}$ (C/m^3), on the electrode. The initial condition for Equation 4 is $\rho_c = 0$ (C/m^3).

The computations for the circular cross section used a structured grid, but those for the triangle employed both a structured and an unstructured grid. For the triangle with structured mesh, the electrode was excluded from the channel and the boundary conditions of $V = V_e$ (kV) and $\rho_c = \rho_{c,e}$ (C/m^3), both at the electrode, were given to the problem as sources applied to a cell at the center of the channel. The use of a source term for assigning a fixed value to a specific point in the solution domain is a common approach and is clearly described by Patankar [21].

Equations 3 and 4 were solved simultaneously. The value of charge density at the electrode, $\rho_{c,e}$, was initially guessed. With this guessed value, Equations 3 and 4 were solved together to obtain the distribution of electric potential and charge density for the entire cross section. Then, the corona current per unit length of the channel was determined from the computations as follows:

$$I = -\int \rho_c b \frac{\partial V}{\partial n} d\ell. \tag{5}$$

In this equation, 'n' is the independent space variable perpendicular to the equipotential lines, such as the walls. It is positive in the direction from the electrode towards the walls. Therefore, the potential gradient is negative, giving a positive value for the corona current.

An experimental setup was designed and fabricated to generate and measure the corona current inside the circular tube and triangular duct. Details of the setup and experimental procedure are available in [16,22].

The integration in Equation 5 is carried out on the periphery of the channel cross section. The electric current, obtained from the computations based on Equation 5, is then compared with the experimental current. If the calculated and measured currents were equal, the initial guess of the charge density was correct and the electric field was obtained.

The flow field is governed by the continuity, momentum and energy equations written compactly in Cartesian tensor notation as follows:

$$\partial_i u_i = 0, \tag{6}$$

$$\partial_o u_i + u_j \partial_j u_i = -\frac{1}{\rho}\partial_i P + \nu \partial_j \partial_j u_i + \frac{\rho_c}{\rho} E_i + g\beta(T - T_o)\delta_{i2}, \tag{7}$$

$$\partial_o T + u_j \partial_j T = \alpha \partial_j \partial_j T. \tag{8}$$

These equations are for two-dimensional, transient flows with Boussinesq approximation for density as $(\rho_0 - \rho) = \rho\beta(T - T_0)$. The equations are coupled via the buoyancy term, which appears as the last term in Equation 7. The subscript '2' in δ_{i2} refers to the 'y' axis, which points vertically upward. The third term on the right side of Equation 7 represents the electric body force, which is found from the solution of the electric field equations.

The boundary conditions for Equations 6 to 8 are no-slip (zero velocity) on the channel walls and on the electrode surface, isothermal on the left and right walls, and adiabatic (zero temperature gradient) on the bottom wall. These equations were solved to obtain the velocity and temperature fields.

The average rate of heat transfer for one wall is used to define the heat transfer coefficient as follows:

$$\dot{Q} = hA(T_h - T_c). \tag{9}$$

In this equation, 'h' is the average heat transfer coefficient for combined convection, which is obtained when the flow is generated by the simultaneous effects of electric and thermal buoyancy body forces. The area 'A' is the area of one wall of the channel. With this definition, $\dot{Q}$ is the rate of heat transfer from one wall. In the absence of electric body force (pure natural convection), the heat transfer coefficient is represented by 'h_0', defined as in Equation 9. The local heat transfer coefficients to be reported later in this paper are obtained from Equation 9 after replacing $\dot{Q}/A$ by the local heat flux. Like the average coefficients, the local coefficients are also based on the wall-to-wall temperature difference of $T_h - T_c = 2$ K.

The convective heat transfer coefficients are written in terms of Nusselt number, defined as $\mathrm{Nu} = hD_h/k$ and $\mathrm{Nu}_0 = h_0 D_h/k$ for the combined and natural convections, respectively. With this definition, the enhancement of combined heat transfer relative to natural convection is indicated by $\mathrm{Nu}/\mathrm{Nu}_0$. Considering Equation 9, it is clear that $\mathrm{Nu}/\mathrm{Nu}_0 = h/h_0 = \dot{Q}/\dot{Q}_0$. Therefore, enhancement of Nusselt number implies enhancement of the rate of heat transfer.

ANALYTICAL SOLUTION FOR THE CIRCULAR TUBE

The electrodynamics equations, Equations 3 and 4, can be solved analytically for the circular cross section. Since the geometry and boundary conditions are symmetric, the potential and charge density distributions are azimuthally symmetric. It can be shown that distribution of the charge density from the analytical solution [19] is as follows:

$$\rho_c = -\frac{I}{2\pi r b(dV/dr)}, \tag{10}$$

where the radial potential gradient is:

$$\frac{dV}{dr} = -\sqrt{\frac{I}{2\pi b\varepsilon} + \frac{C_1}{r^2}}, \tag{11}$$

where $C_1 = 1,242,088.9$, electrical current is $I = 0.66$ mA, ion mobility for air is $b = 10^{-4}$ m^2/V.s and permittivity is $\varepsilon = 8.8542 \times 10^{-12}$ F/m. With these values, the electric charge density can be plotted as a function of radial coordinates. This analytical solution is used to validate the computational results.

COMPUTATIONAL METHOD

The governing equations were discretized on either structured or unstructured mesh using a finite-volume method. Figure 2 shows the three different meshes used in the present computations. Details of discretization may be found in [21,23].

The mesh for the circular cross section was structured. It was constructed from radial and circular lines; the lines were clustered near the electrode and near the wall. In the meshing process, the volume of the electrode was excluded from the computational domain, and the boundary conditions were applied at the surface of the electrode.

Unlike the circular cross section, the mesh for the triangular cross section was either structured or unstructured. The diagram 'b' in Figure 2 shows the unstructured mesh. The mesh is constructed from triangular cells, clustered near the electrode and approximately uniform farther away. As in the circular cross section, the volume of the electrode was excluded from the computational domain and the boundary conditions were applied at the surface of the electrode.

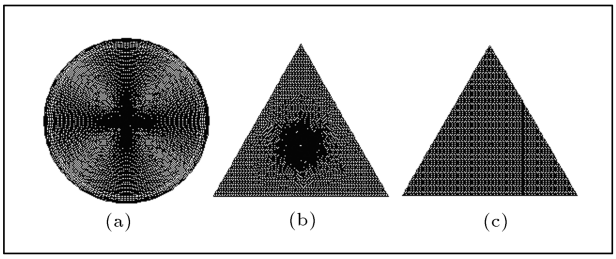

Figure 2. Different meshes of the present computations; (a) structured, (b) unstructured, and (c) structured.

The structured mesh of the triangular cross section is shown in diagram 'c' of Figure 2. As seen in the diagram, the mesh is uniform throughout the domain, constructed from equilateral triangular cells. The electrode here is simulated by assigning the electrode voltage and charge density to the cell, located at the geometric center of the cell, using a source term [21]. The uniform mesh proved to be very effective in providing a good solution, in which the contours of charge density and body force are smooth and symmetric.

Although the diagrams of Figure 2 are representative, the actual meshes employed in the computations, as detailed in Table 1, had 12000 cells for the circular cross section and 10000 and 7000 cells for the structured and unstructured meshes of the triangular cross section, respectively.

The computations were performed with FLUENT software. A User-Defined-Function (UDF) was written in C language and was linked to FLUENT to solve the electrodynamic field equations (Equations 3 and 4). The second-order upwind scheme was used for the potential (Equation 3) and the charge density (Equation 4) equations. The SIMPLE algorithm was used to provide the pressure-velocity coupling, and the second order upwind scheme was used to solve the momentum and energy equations.

The convergence criteria were to reduce the residuals of various equations to less than certain values. For the continuity, momentum, energy, potential and charge density equations, the computations were continued until the residuals were less than 10^{-10}, $(10^{-10} - 10^{-9})$, $(10^{-12} - 10^{-11})$, $(10^{-17} - 10^{-10})$, and $(10^{-15} - 10^{-10})$, respectively. Table 1 shows the details for each case. These small values ensured that the iterative solutions were fully converged. The potential and charge density equations were solved as an unsteady problem with the first order implicit method for time. The flow and temperature field equations, however, were solved with either unsteady or steady formulation, depending on the case. All the computations were performed on the two-dimensional geometry.

Table 1. Mesh structure and convergence residuals.

Geometry	Gas	Mesh	No. of Cells	Continuity	Momentum	Energy	Potential	Charge Density
Circle	Air	Structured	12000	-	-		10^{-17}	10^{-15}
Triangle	Nitrogen	Unstructured	7000	-	-		10^{-10}	10^{-11}
Triangle	Air	Unstructured	7000	10^{-10}	10^{-10}	10^{-12}	10^{-11}	10^{-12}
Triangle	Nitrogen	Structured	10000	10^{-10}	10^{-9}	10^{-11}	10^{-10}	10^{-10}

GRID REFINEMENT STUDIES

The computations for the circular cross section were performed on three different grids to examine the effect of grid density on the solution. Figure 3 is the plot of the dimensionless electric charge density for 600-1200 and 12000-cell grids. The analytical solution derived earlier is also shown as a basis for comparison. In Figure 3, the abscissa, r/R, is the radial distance from the electrode normalized by the radius of the cross section. The ordinate is the dimensionless charge density, $(\rho_c - \rho_{c,w})/(\rho_{c,e} - \rho_{c,w})$, where ρ_c is the azimuthally-averaged charge density at radial position r. The charge density, $\rho_{c,e}$, represents the value on the electrode (0.000942 C/m^3), and $\rho_{c,w}$ shows the value on the wall (0.000300 C/m^3).

As seen in the figure, there is a good agreement between numerical and analytical results, except for the locations with $r/R < 0.15$ near the electrode. The numerical solution, however, is improved as the number of grid cells is increased. The small imperfections of the solution for the 12000-cell grid very near the electrode are reminiscent of the present second-order method.

It is to be noted that analytical solution is available only for the circular cross section and not for the triangle. However, the computational approach is the same for both geometries. Therefore, the present grid study not only confirms the validity of the results for the circle, it also supports the computations of the triangle. Grid refinement studies were also performed for the triangle with both structured and unstructured grids. A sample plot is shown in Figure 4, and more details are available in [22]. It is noteworthy that

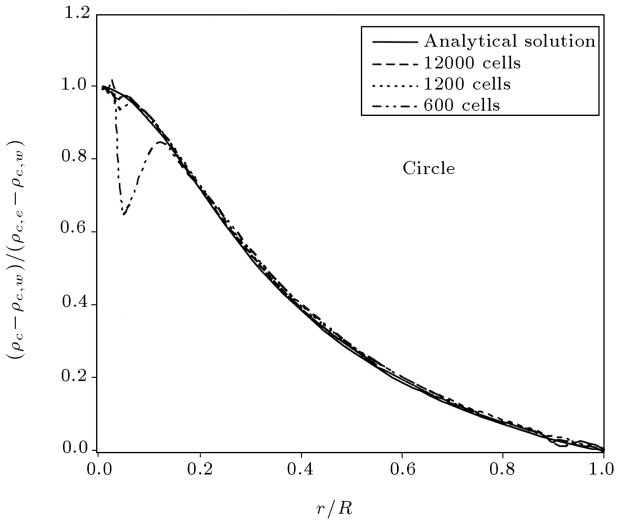

Figure 3. Grid study for the azimuthally-averaged values of electric charge density in the circular geometry for corona discharge in air; Pe $= \infty$, $\rho_{c,e} = 0.000942$ and $\rho_{c,w} = 0.000300$ C/m^3.

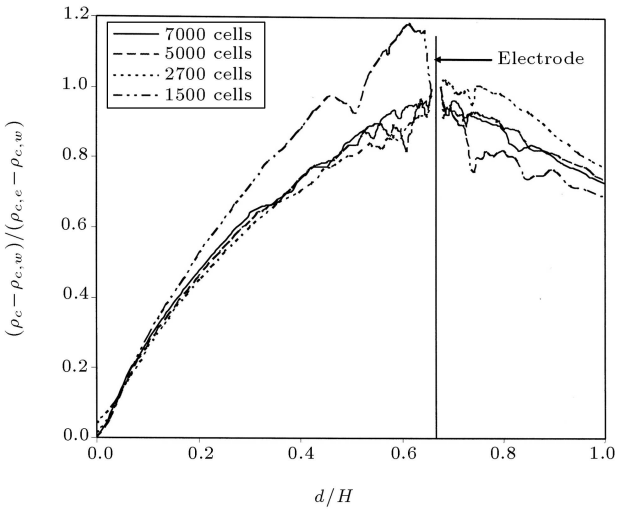

Figure 4. Grid study for the distribution of charge density on a vertical line in the triangular geometry for the applied voltage of 8.5 kV using the unstructured grid; Pe $= \infty$, $\rho_{c,e} = 0.000208$ and $\rho_{c,w} = 0.0000133$ C/m^3.

the results of the grid study for the electric potential are much smoother than that for the charge density. Moreover, the grid study performed on the structured grid is much smoother than the unstructured grid.

RESULTS AND DISCUSSION

In this section, a major shortcoming of the numerical solution of electrodynamics and flow equations is revealed and two remedies are recommended. This is accomplished by paying especial attention to the solution of the charge density equation. It is shown that the correct solution of the charge density is essential in obtaining a reliable prediction of the heat transfer enhancement in corona wind applications.

Shortcomings of the Solution

The computation of charge density for the circular cross section is expected to be azimuthally symmetric. This expectation comes from the fact that the geometry and boundary conditions of the circle are azimuthally unvarying. This characteristic of the corona discharge in the circular tubes can be used to examine the validity of the computational approach.

The upper plot of Figure 5 presents the local charge density for the circular cross section versus radial distance from the electrode. The ordinate and abscissa are both in dimensionless form. Normally, plotting the results along a radial line should be sufficient - expecting the plots along all other radii to yield the same distribution because of the azimuthal symmetry. Nevertheless, the values for all the grid points of the mesh are included in the plot, in order to see whether the solution satisfies the expected

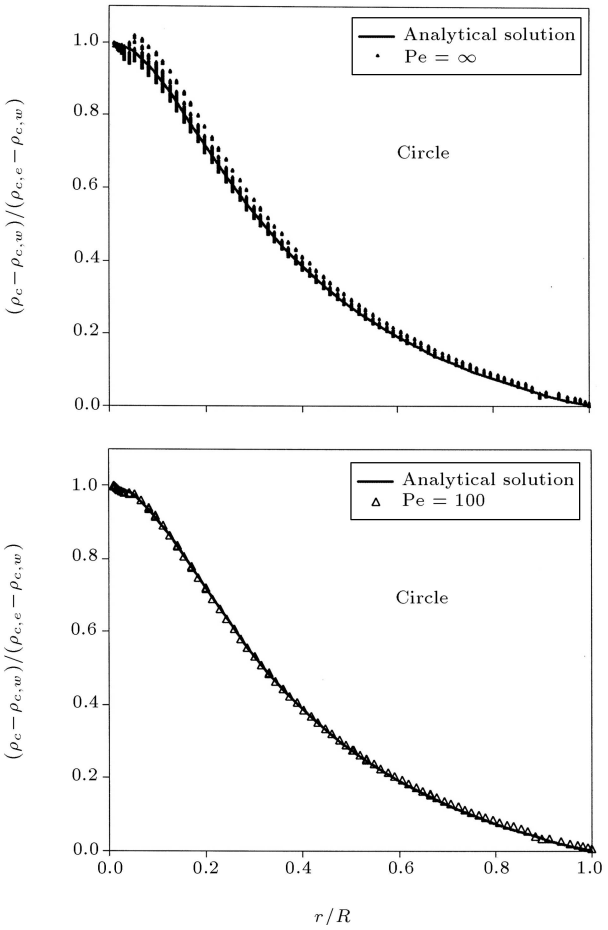

Figure 5. Electric charge density of all points for corona discharge in air inside the circular duct with no artificial viscosity (top) and localized artificial viscosity (bottom); $\rho_{c,e} = 0.000942$ and $\rho_{c,w} = 0.000227$ C/m^3.

symmetry. As seen in the figure, the points for the same radial position, but different azimuthal locations, do not coincide. The points are closer together near the wall (larger values of r/R), and they spread out and move farther apart near the electrode. A correct numerical solution should have no data spread and should coincide with the analytical solution. On the contrary, the present computations have generated results that, when plotted along different radial lines, appear as a cloud of points about the analytical curve. It can be shown that this shortcoming of the computation can be improved by including a judicious amount of artificial viscosity in the charge density equation.

A Remedy - the Use of Artificial Viscosity

To improve the foregoing deficiency, the charge density equation is revised to include a diffusion term as follows:

$$\partial_o \rho_c + \partial_i(-\rho_c b \partial_i V) = \partial_i(\Gamma \partial_i \rho_c). \qquad (12)$$

In this equation, the diffusion term on the right, with artificial viscosity Γ, has been added to control the solution. The artificial viscosity is determined from the Peclet number, defined either as $\mathrm{Pe} = bV_e/\Gamma$ for a uniform value of Γ or $\mathrm{Pe} = bEL/\Gamma$ for the local values of Γ. In the first definition, Γ is a fixed value for the entire computational domain. In the latter, Γ is the locally calculated artificial viscosity for a fixed value of Pe and its value depends on the local intensity of the electric field. The latter procedure ensures that a large artificial viscosity is applied near the electrode and a smaller value near the wall. The Peclet number indicates the relative importance of the convection and diffusion terms. A large Pe corresponds to a small diffusion. In other words, $\mathrm{Pe} = \infty$ in the upper plot of Figure 5 implies $\Gamma = 0$, that is, no artificial viscosity. And a finite value of Pe, such as $\mathrm{Pe} = 100$ in the lower plot of Figure 5, indicates a non-zero, yet small value of the artificial viscosity, Γ.

The lower plot of Figure 5 is obtained from Equation 12, with local values of artificial viscosity corresponding to the Peclet number of $\mathrm{Pe} = 100$. Since Pe depends on the local intensity of the electric field, the constant value of $\mathrm{Pe} = 100$ assigns a large artificial viscosity near the electrode where the electric field intensity is high. On the other hand, the data spread is larger near the electrode, where a larger artificial viscosity is needed. This local assignment of artificial viscosity is, therefore, consistent with the shortcoming of the solution. As seen in Figure 5, the data spread is drastically reduced and the data points are almost coincident with the analytical solution.

Since neither analytical solution nor experimental data is available for the triangular cross section, the impact of artificial viscosity on the charge density distribution cannot be evaluated for the triangle as clearly as for the circle. However, similar computations for the triangle with artificial viscosity indicate that the distribution of charge density along the three different heights of the triangle becomes nearly the same [22].

A convenient way to visualize the effect of dispersion error on the solution is the contour plots of Figure 6. The left and right columns of each cross section correspond to the uniform and local treatments of the artificial viscosity, respectively. The case of $\mathrm{Pe} = \infty$ has no artificial viscosity and clearly shows the azimuthal nonuniformity for the circular cross section. This leads to a nonuniform electric body force that, if used in the flow equations, will lead to a disturbed and perhaps erroneous flow field.

The favorable smoothing effect of artificial viscosity increases as Pe is decreased. The best case is obtained for $\mathrm{Pe} = 100$ and the worst corresponds to $\mathrm{Pe} = 1$. A careful examination of the contours on the left and right columns for each geometry shows

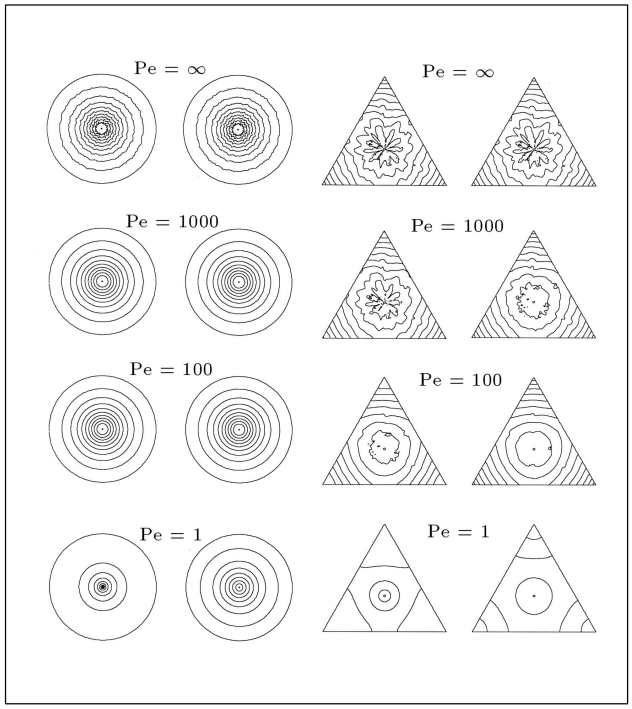

Figure 6. Contour lines of dimensionless charge density; ten contour lines are plotted from zero to one; the left and right diagrams of each geometry are, respectively, for uniform and localized artificial viscosity; circle: Corona discharge in air, $\rho_{c,e} = 0.000942$ and $\rho_{c,w} = 0.000227$ C/m^3; triangle: Corona discharge in nitrogen, $\rho_{c,e} = 0.000208$ and $\rho_{c,w} = 0.0000133$ C/m^3.

that the local assignment of artificial viscosity is more effective. Unlike the circular geometry, the values of charge density on the walls of the triangle decrease from the middle of the wall towards the vertices. The largest values occur in the middle and the smallest values are at the vertices.

The selection of Pe = 100 as the best case is subject to interpretation. To obtain this value, four different values of Pe were considered, namely, Pe = 1, 100, 1000, and ∞. The computations for a circular tube with a local assignment of artificial viscosity indicated that the dimensionless charge density, $(\rho_c - \rho_{c,w})/(\rho_{c,e} - \rho_{c,w})$, is 0.825, 0.891, 0.899, and 0.895, respectively, for Pe = 1, 100, 1000, and ∞. From an analytical solution of the circular tube, the value is 0.891, which is the same as the computational value obtained for Pe = 100. This justifies the validity of Pe = 100 as the best value for the circular tube. For the triangular duct, however, the analytical solution is not available, and one has to rely on the contour plots of Figure 6. Therefore, the value Pe = 100 should not been viewed in an exact mathematical context. However, this value seems to provide the best result for both circular and triangular cross sections within the discrete values of Pe considered in this investigation.

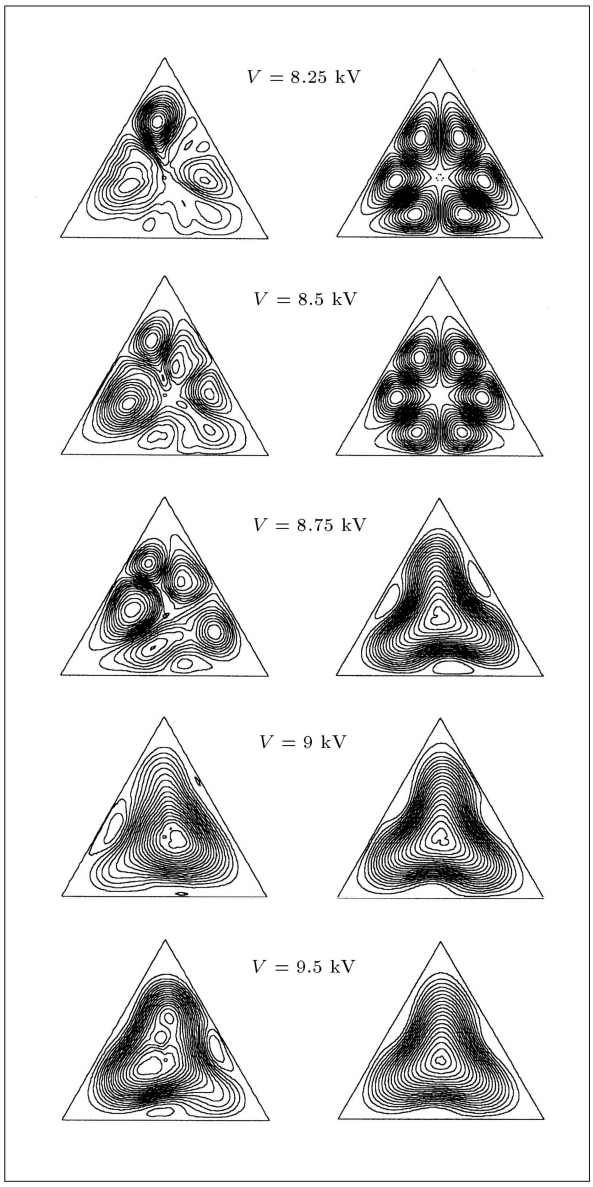

Figure 7. Streamlines of corona discharge in nitrogen gas for the unstructured (left) and the structured (right) grids.

An Alternative Remedy - the Use of Structured Grid

Another approach for improving the numerical solution of the charge density equation is using a structured mesh. To show the remedial impact of the structured mesh, the flow streamlines obtained with the structured and unstructured meshes are compared in Figure 7. Here, the thermal buoyancy effect is absent, and the flow is generated by the electric body force, that is, the flow is only the corona wind. The left plots are obtained from the unstructured mesh, while the right plots are for the structured mesh.

As seen in the figure, the flow has multiple vortices at lower values of the applied voltage. It is clear that the contour lines for the structured grid

are well-organized and symmetric - consisting of six vortices. The unstructured gird, on the other hand, has a hard time resolving the multi-vortex and symmetric nature of the problem; the flow seems to be chaotic. At higher voltages, however, the flow transits into a large recirculation with small vortices pressed against the walls. Even at these higher voltages, the expected symmetry, disturbed by the unstructured mesh, is effectively restored by the structured mesh.

More evidence of the favorable effect of structured mesh on the solution of the electrodynamics and flow equations is given in Figure 8. The top three rows of diagrams in Figure 8 are for unstructured mesh, while the last row at the bottom is for the structured mesh. Comparison of the diagrams clearly shows the favorable effect of the structured mesh. The irregular contours of charge density and the asymmetric streamlines seen in the top row are totally eliminated in the bottom diagrams with the structured mesh.

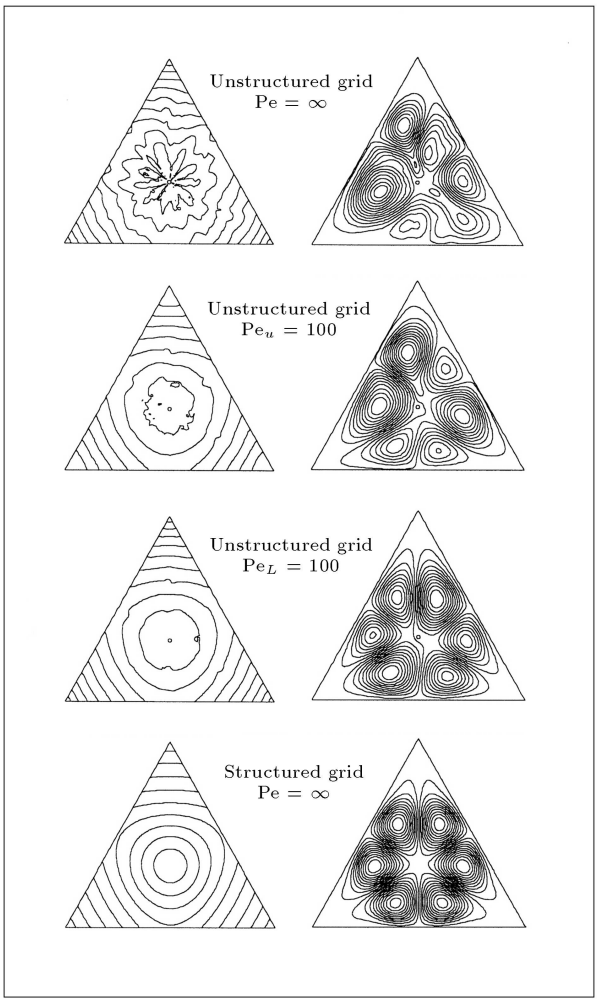

Figure 8. Contours of charge density on the left and streamlines of corona wind on the right; $V = 8.5$ kV.

Heat Transfer Enhancement and Flow Transition

The impact of the aforementioned flow patterns on natural convection heat transfer in the triangular duct for nitrogen gas is presented in Figure 9. In this figure, the abscissa is the voltage applied to the electrode and the ordinate is the heat transfer enhancement represented by the ratio of Nusselt number for the combined convection (natural convection + corona wind) to that for pure natural convection driven by thermal buoyancy. The results are plotted for the structured as well as the unstructured grids. The gap in each curve represents a jump in the value of enhancement, because the flow pattern changes from the multi-vortex pattern to a single large recirculation.

As seen in Figure 9, enhancement obtained from the structured and unstructured grids range from (17.9% to 106.9%) and (34.5% to 126.8%), respectively. The enhancement predicted by the structured gird is somewhat lower than that obtained from the unstructured grid. Since the structured grid seems to give smoother and more even solution, it is safer to rely on the enhancements obtained from the structured grid.

The flow pattern has a marked effect on enhancement. The results from the structured grid show that the enhancement jumps from 43.6% to 74.5% when the flow pattern is changed. With the limited results obtained in the present computations, it is not clear exactly when the flow pattern undergoes a change. Further studies are needed to determine whether the enhancement jump in this region is, indeed, due to a changed flow pattern.

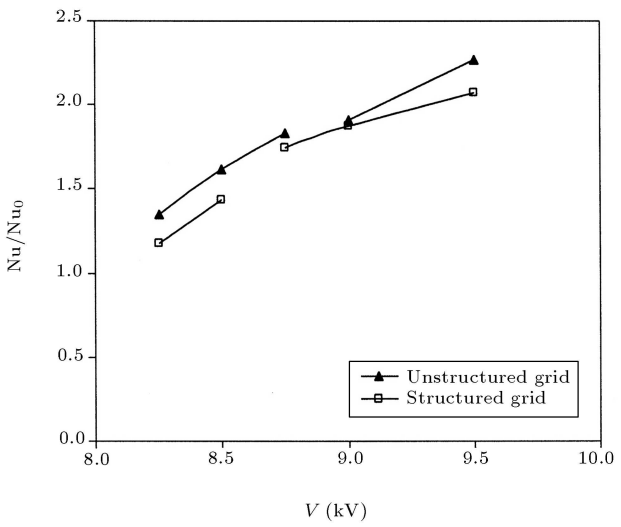

Figure 9. Effect of applied voltage on enhancement of natural convection by corona discharge in nitrogen gas inside the triangular duct; Ra = 3737.

Enhancement as Affected by Thermal Boundary Condition

Figure 10 presents the enhancement of heat transfer for different values of Rayleigh number, Ra, for corona discharge in air for the triangular duct with unstructured grid. The ordinate, Nu/Nu_0, is the ratio of wall-averaged Nusselt number for the combined flow over that for pure natural convection for the same value of Ra. Two cases are shown in the figure. One is for the hot wall located on the right; the other is when the hot wall is located on the left. Near the hot wall, the thermal buoyancy body force is acting upward, while, near the cold wall, it is downward. This generates a torque, in either a counterclockwise or clockwise direction. The electric body force, on the other hand, is nearly always radial, directed from the electrode towards the walls. It is the interaction of these two body forces that determines the flow. The solid lines in Figure 10 represent the best fit to the data.

According to Figure 10, the heat transfer enhancement is better at the lower values of Ra, where more enhancements is needed and the level of enhancement decreases as Ra is increased. It is noteworthy that the flow circulation driven by thermal buoyancy is more intense at higher values of Ra. However, the flow at higher Ra is not transporting thermal energy of the hot wall to the cold wall as efficiently as the flow at lower Ra. This implies the favorable effect of the corona wind and the adverse effect of the buoyancy in the combined mode.

The enhancement of local heat transfer for corona discharge in air inside the triangular duct is presented in Figure 11. The local heat transfer coefficient is defined, based on local wall heat flux and the temperature difference of the hot and cold walls (2 K). The local Nusselt number is defined, based on the local heat transfer coefficient and the hydraulic diameter of the triangular duct. The overall Nusselt number for pure natural convection, Nu_0, is evaluated at the corresponding value of Ra. Figure 11 shows the effect of Ra for a fixed value of the applied voltage. Two sets of plot are presented in this figure - one for the hot wall, the other for the cold wall. To avoid mixing the results, the curves of the cold wall are plotted below the horizontal axis on the negative side. Nevertheless, it should be noted that this is done for convenience, and only the absolute value of the enhancements should be used. The abscissa in the figure is the vertical distance from the adiabatic wall.

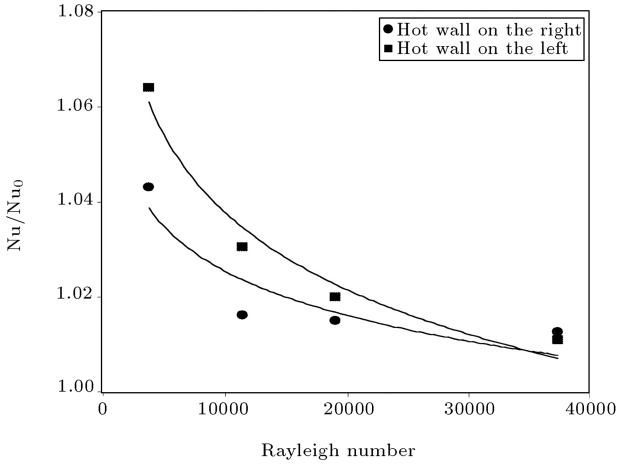

Figure 10. The enhancement of natural convection by corona discharge in air inside the triangular duct with unstructured grid; the electrode voltage and charge density are 7.5 kV and 2.5×10^{-5} C/m^3.

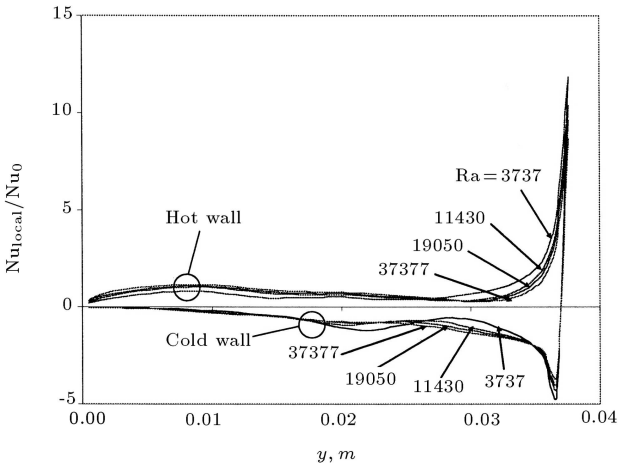

Figure 11. Enhancement of the local Nusselt number on the hot and cold walls for corona discharge in air inside the triangular duct with unstructured grid; the applied voltage and electrode charge density are 7.5 kV and 2.5×10^{-5} C/m^3.

Review of Figure 11 indicates a mild variation of the local enhancement for most of the length of the walls except near the apex of the cross section. Among the curves plotted for the fixed applied voltage of 7.5 kV, the curve corresponding to Ra = 3737 is somewhat separate from the other curves as the electric body force is more influential at this relatively low value of Ra. It is evident from the figures that the complex flow field generated by the combined effects of thermal buoyancy and electric body force with the multi-vortex flow pattern discussed earlier has contributed to the local variations of the heat transfer enhancement along the walls.

CONCLUDING REMARKS

This research discussed the shortcomings of the numerical solution in using corona discharge in circular tubes and triangular ducts and recommended remedies for improvement. It indicated that the numerical solution

of electrodynamics equations may lead to imperfect values of charge density. The difficulty arises from dispersion errors, due to the absence of a diffusion term in the charge density differential equation. It could also arrive from the use of an unstructured grid. It was indicated that the solution is improved by adding a small amount of artificial viscosity to the charge density equation.

The computations were performed for the circular and triangular geometries with structured and unstructured grids, respectively. The amount of artificial viscosity was controlled via the Peclet number. In this study, the solution for Pe = 100 showed a promising result for charge density, and that of Pe = 1 degenerated the solution.

Local treatment of the artificial viscosity proved to be effective. This approach applied larger artificial viscosity near the electrode and smaller values near the walls.

The most important effect of the dispersion error was the azimuthal nonuniformity of the charge density and the resulting electric body force. As a consequence, the nonuniform electric body force disturbs the flow and upsets the symmetric flow patterns that may exist in certain geometries. The corona discharge in a triangular geometry is expected to give symmetric flow patterns consisting of pairs of vortices; these patterns may not materialize if the solution of the electrodynamics equations provides a nonuniform charge density. This implies that the flow patterns obtained when the equations are solved for a portion of the geometry (symmetry imposed beforehand) will be different from those obtained when the equations are solved for the whole geometry.

In addition, the study revealed many complex features of combined corona wind and natural convection in triangular channels. It was found that flow is comprised of six vortices at lower voltages. At higher voltages, the flow pattern changes into large recirculation with small vortices near the walls. The computations indicated that, at lower Rayleigh numbers, the electric body force dominates and has more impact on heat transfer. For Ra = 3737 and 8.25 kV $\leq$ V $\leq$ 9.5 kV, the heat transfer enhancement, based on the structured grid, was from $\mathrm{Nu}/\mathrm{Nu}_0 = 1.179$ to 2.069, or 17.9-106.9%.

NOMENCLATURE

A	area of one side of the channel, m^2
b	ion mobility, 10^{-4} m^2/V.s (air), 2.37×10^{-4} m^2/V.s (nitrogen)
C_p	specific heat of nitrogen gas, 1040.67 J/kg.K
D	diameter of the circular cross section, 25.4 mm
D_i	displacement vector, C/m^2
D_h	hydraulic diameter of the triangle, 25.4 mm, 17.32 mm
d	electrode diameter, 0.254 mm, 0.5 mm
E_i	electric field intensity, V/m
g	acceleration of gravity, m/s^2
H	height of the triangular cross section, 38.1 mm, 25.98 mm
h	heat transfer coefficient for combined convection, W/m^2.K
h_0	heat transfer coefficient for natural convection, W/m^2.K
i	index, $i = 1, 2, 3$ for x, y and z directions
I	electric current per unit length, A/m
J_i	electric current density, A/m^2
k	thermal conductivity of nitrogen gas, 0.0242 W/m.K
ℓ	space variable along equipotential lines
L	base length of the triangular cross section, 44 mm, 30 mm
n	space variable perpendicular to equipotential lines
Nu	Nusselt number for combined convection, hD_h/k
Nu_0	Nusselt number for natural convection, $h_0 D_h/k$
P	gas pressure, Pa
Pe	Peclet number, Pe $= bV_e/\Gamma$ or bEL/Γ
$\dot{Q}$	rate of heat transfer from one wall of the channel, W
Ra	Rayleigh number, Ra $= g\beta(T_h - T_c)D_h^3/\alpha\nu$
t	time, s
T	temperature, K
T_c	temperature of the cold wall, 300 K
T_h	temperature of the hot wall, 302 K
T_0	reference temperature, 301 K
u	velocity, m/s
u_i	velocity component, m/s
V	electric potential, V
V_e	electric potential applied to the electrode, V

Greek Symbols

α	thermal diffusivity of nitrogen gas, $k/\rho C_p$, 1.96289×10^{-5} m^2/s

β	coefficient of nitrogen gas, 1/T, 0.0033 1/K
δ_{ij}	Kronecker delta, 0 or 1
ε	permittivity, 8.8542×10^{-12} F/m
ν	kinematic viscosity of nitrogen gas, 1.461 m^2/s at 1 atm and 300 K
ρ	density of nitrogen gas, 1.138 kg/m^3 at 1 atm and 300 K
ρ_c	space charge density, C/m^3
$\rho_{c,e}$	space charge density on the electrode, C/m^3
$\rho_{c,w}$	space charge density on the wall, C/m^3
σ	electrical conductivity, S/m
∂_i	partial differentiation with respect to x_i, $\partial()/\partial x_i$
∂_0	partial differentiation with respect to time, $\partial()/\partial t$

Subscripts

c	electric charge
e	electrode
w	wall

REFERENCES

1. Ohadi, M.M., Nelson, D.A. and Zia, S. "Heat transfer enhancement of laminar and turbulent pipe flow via corona discharge", *International Journal of Heat and Mass Transfer*, **34**(4-5), pp 1175-1187 (1991).
2. Ohadi, M.M., Sharaf, N. and Nelson, D.A. "Electrohydrodynamic enhancement of heat transfer in a shell-and-tube heat exchanger", *Experimental Heat Transfer*, **4**(1), pp 19-39 (1991).
3. Tada, Y., Takimoto, A. and Hayashi, Y. "Heat transfer enhancement in a convective field by applying ionic wind", *Journal of Enhanced Heat Transfer*, **4**(2), pp 71-86 (1997).
4. Franke, M.E. and Hodge, P.R.C. "Corona wind cooling of horizontal cylinders in air", *Proceedings of the ASME-JSME Thermal Engineering Joint Conference*, **4**, pp 261-267 (1995).
5. Lai, F.C. "Effects of buoyancy on electrohydrodynamic-enhanced forced convection in a horizontal channel", *Journal of Thermophysics and Heat Transfer*, **12**(3), pp 431-436 (1998).
6. Kalman, H. and Sher, E. "Enhancement of heat transfer by means of a corona wind created by a wire electrode and confined wings assembly", *Applied Thermal Engineering*, **21**(3), pp 265-282 (2001).
7. Wangnipparnto, S., Tiansuwan, J., Jiracheewanun, S., Kiatsiriroat, T. and Wang, C.C. "Air side performance of thermosyphon heat exchanger in low Reynolds number region: With and without electric field", *Energy Conversion and Management*, **43**(14), pp 1791-1800 (2002).
8. Nelson, D.A., Zia, S., Whipple, R.L. and Ohadi, M.M. "Corona discharge effects on heat transfer and pressure drop in tube flows", *Enhanced Heat Transfer*, **7**, pp 81-95 (1998).
9. Takimoto, A., Tada, Y., Hayashi, Y. and Yamada, K. "Convective heat transfer enhancement by a corona discharge", *Heat Transfer: Japanese Research*, **20**(1), pp 18-35 (1991).
10. Blanford, M.D., Ohadi, M.M. and Dessiatoun, S.V. "Compound air-side heat transfer enhancement in a cross-flow refrigerant-to-air heat exchanger", *ASHRAE Transactions*, **101**(2), pp 1049-1054 (1995).
11. Yang, H. and Lai, F.C. "Effects of Joule heating on EHD-enhanced natural convection in an enclosure", *Conference Record of the IEEE Industry Applications*, **3**, pp 1851-1858 (1997).
12. Molki, M., Ohadi, M.M., Baumgarten, B., Hasegawa, M. and Yabe, A. "Heat transfer enhancement of airflow in a channel using corona discharge", *Enhanced Heat and Mass Transfer*, **7**, pp 411-425 (2000).
13. Ngo, C.C. and Lai, F.C. "Effects of electric field on natural convection in an enclosure heated from below", *Proceedings of the 35th National Heat Transfer Conference*, Anaheim, CA, pp 1-8 (2001).
14. Tan, K.T. and Lai, F.C. "EHD-enhanced natural convection in an enclosure: Effects of non-symmetric electric field", *Proceedings of the 35th National Heat Transfer Conference*, Anaheim, CA, pp 1-9 (2001).
15. Kasayapanand, N., Tiansuwan, J., Asvapoositkul, W., Vorayos, N. and Kiatsiriroat, T. "Effect of the electrode arrangements in a tube bank on the characteristics of electrohydrodynamic heat transfer enhancement: Low Reynolds number", *Journal of Enhanced Heat Transfer*, **9**(5-6), pp 229-242 (2002).
16. Molki, M. and Bhamidipati, K.L. "Enhancement of convective heat transfer in the developing region of circular tubes using corona wind", *International Journal of Heat and Mass Transfer*, **47**(19-20), pp 4301-4314 (2004).
17. Molki, M. and Damronglerd, P. "Electrohydrodynamic enhancement of heat transfer for developing air flow in square ducts", *Heat Transfer Engineering*, **27**(1), pp 35-45 (2006).
18. Molki, M. and Harirchian, T. "The enhancement effect of corona discharge on natural convection heat transfer in triangular channels", *Paper IMECE2005-80070, Proceedings of IMECE2005, ASME International Mechanical Engineering Congress and Exposition*, Orlando, Florida, USA (2005).
19. Molki, M. and Harirchian, T. and Chitta, V.L. "An improved solution of electrodynamics equations for corona discharge using explicit artificial viscosity", *Numerical Heat Transfer*, Part B, pp 315-332 (2006).

20. Molki, M. and Harirchian, T. "Enhancement of natural convection heat transfer in triangular channels using corona discharge in nitrogen gas", *ASME International Mechanical Engineering Congress and Exposition*, Chicago, Illinois, USA (2006).

21. Patankar, S.V., *Numerical Heat Transfer and Fluid Flow*, Hemisphere Publishing Corporation, Philadelphia, PA, USA (1980).

22. Harirchian, T., *Enhancement of Convective Heat Transfer in Triangular Channels Using Corona Discharge in Nitrogen Gas*, MS Thesis, Southern Illinois University of Edwardsville, Edwardsville, Illinois, USA (2006).

23. *Fluent 6.2 User's Guide*, Fluent Inc., Lebanon, New Hampshire (2005).